

# A $\pm 0.5$ -mV-Minimum-Input DC-DC Converter with Stepwise Adiabatic Gate-Drive and Efficient Timing Control for Thermoelectric Energy Harvesting

Eric J. Carlson, Joshua R. Smith

**Abstract**— This paper presents a step-up DC-DC converter that uses a stepwise gate-drive technique to reduce the power FET gate-drive energy by 82%, allowing positive efficiency down to an input voltage of  $\pm 0.5$  mV—the lowest input voltage ever achieved for a DC-DC converter as far as we know. Below  $\pm 0.5$  mV the converter automatically hibernates, reducing quiescent power consumption to just 255 pW. The converter has an efficiency of 63% at  $\pm 1$  mV and 84% at  $\pm 6$  mV. The input impedance is programmable from 1  $\Omega$  to 600  $\Omega$  to achieve maximum power extraction. A novel delay line circuit controls the stepwise gate-drive timing, programmable input impedance, and hibernation behavior. Bipolar input voltage is supported by using a flyback converter topology with two secondary windings. A generated power good signal enables the load when the output voltage has charged above 2.7 V and disables when the output voltage has discharged below 2.5 V. The DC-DC converter was used in a thermoelectric energy harvesting system that effectively harvests energy from small indoor temperature fluctuations of less than 1°C. Also, an analytical model with unprecedented accuracy of the stepwise gate-drive energy is presented.

**Index terms**—Energy harvesting, DC-DC converter, bipolar, flyback converter, low-voltage, low-power, adiabatic gate-drive, stepwise gate-drive, charge recycling, thermoelectric generator.

## I. INTRODUCTION

IN recent years, many works have proposed using thermoelectric generators (TEGs) [1] to power wireless devices from heat sources. Some describe using active heat sources such as the human body [2]–[6], trees [7], or vehicles [8]. Others have demonstrated that power can be harvested from the temperature differences that exist between air and structures [9], rocks [10], or soil [11]–[13] due to diurnal fluctuations in air temperature: as the temperature of a mass lags that of the air due to thermal storage. The mass for the thermal storage can be integrated within the energy harvesting unit [14]. Even indoors there is a small amount of thermal energy available from room temperature fluctuations. This paper presents a circuit that can efficiently harvest and store this energy.

A TEG produces a voltage  $V_{\text{TEG}}$  that is proportional to the temperature difference across it  $\Delta T$ , so for the proposed system,

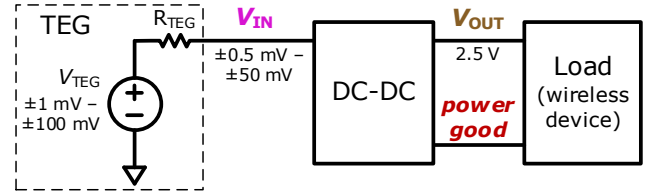


Fig. 1. Energy harvesting system diagram.

the voltage produced by the TEG is small in magnitude and fluctuates in polarity. TEGs can be placed in series electrically to produce more voltage at the expense of higher resistance  $R_{\text{TEG}}$  as done in [14] and [15], but at some point adding more TEGs becomes impractical. Pairing the TEG with a step-up DC-DC converter as in Fig. 1 enables harvesting energy when  $\Delta T$  and  $V_{\text{TEG}}$  are very low. The minimum TEG voltage that can be utilized invariably becomes limited by the DC-DC converter efficiency. A DC-DC converter that can efficiently step up very small voltages of fluctuating polarity is needed.

The DC-DC converter with the lowest reported operational input voltage [5] requires at least 3.5 mV and does not work with negative voltages from the TEG, while the converter with the lowest bipolar operating voltage [16] requires  $\pm 5$  mV. This work proposes a step-up flyback DC-DC converter that has a minimum input voltage of  $\pm 0.5$  mV—ten times lower than the state of the art. This extremely low input voltage is achieved by utilizing a stepwise gate-drive technique that reduces the energy required to drive the gate of the primary power FET  $M_1$  (the dominant source of energy losses) by 82%. Although stepwise gate-drive for inductive DC-DC converters was theorized in [17], until now it was not physically demonstrated in this application. The challenge with successfully implementing a beneficial stepwise gate driver is that the energy required to control the timing signals for each step must not negate the energy savings that stepwise gate-drive provides. To address this, a novel low-power delay line circuit was developed to provide the timing signals for the stepwise gate driver.

The DC-DC converter also needs to be able to match to the source resistance  $R_{\text{TEG}}$  of the TEG for maximum power extraction. The TEG resistance  $R_{\text{TEG}}$  is specific to the material properties of the TEG, the number of TEGs in series, and to the thermal impedance between the TEG and the environment. Making the DC-DC converter input impedance programmable from 1 ohm to 600 ohms allows it to be optimized for a wide range of TEG configurations, including many TEGs in series.

E. Carlson is with the Department of Electrical and Computer Engineering, University of Washington, Seattle, WA and Texas Instruments Inc., Federal Way, WA (e-mail: e2@uw.edu).

J. Smith is with the Allen School of Computer Science and Engineering and the Department of Electrical and Computer engineering, University of Washington, Seattle, WA.

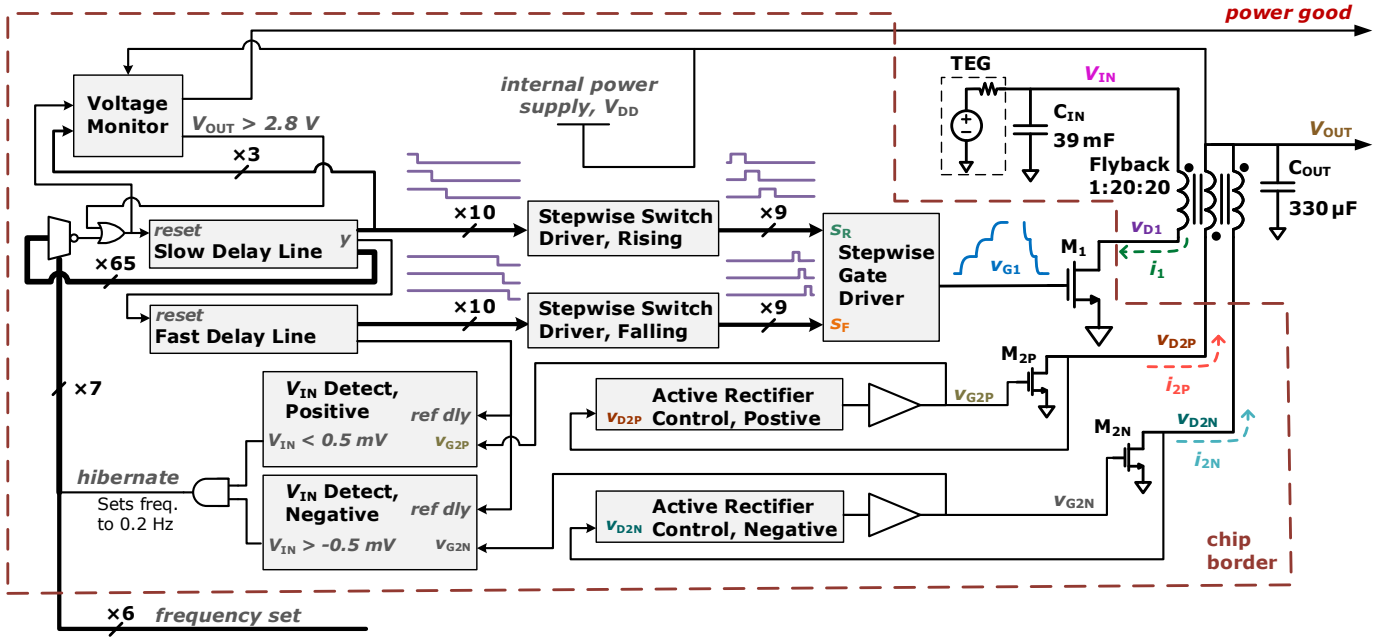


Fig. 2. DC-DC converter block diagram. The 1:20:20 flyback transformer has an inductance of 300  $\mu\text{H}$  on the primary winding.

This is done by leveraging the novel delay line circuit to also set the switching frequency with lots of programmability.

Because the control circuitry cannot operate on just 1 mV, the converter must derive its power supply from its own output. As long as the amount of converted energy per cycle exceeds the power required by the control circuitry, gate drivers, and leakage (including storage capacitors), the output voltage will remain high enough to maintain functionality. If the input power remains too low for too long, then the output voltage will discharge below the minimum level required for operation. Works such as [5],[19],[16],[18] use self-start techniques to recover after this happens. The lowest self-start voltage reported was  $\pm 5\text{ mV}$  and requires special startup circuitry. In this work, with the typical operating voltage of just  $\pm 1\text{ mV}$ , the need for self-start is avoided by putting the DC-DC converter into a low-power hibernation state that sustains  $V_{OUT}$  for several weeks when there is insufficient power available from the TEG. A timing-based technique determines when the input voltage is too low to sustain operation, at which point the switching frequency—controlled by the novel delay line—is reduced to just 0.2 Hz, reducing the total quiescent power to just 255 pW, including capacitor leakage.

## II. DC-DC CONVERTER ARCHITECTURE

The proposed DC-DC converter block diagram is shown in Fig. 2. A flyback transformer with 1:20 turns ratio is used to transfer power from the input  $V_{IN}$  to the output  $V_{OUT}$ . An additional secondary winding of opposite polarity enables bipolar operation. The converter operates in discontinuous conduction mode (DCM), with a fixed but programmable switching frequency.

The primary power FET  $M_1$ , with a resistance of 34 m $\Omega$  and gate capacitance of 250 pF, is the most significant source of power losses in the circuit. A stepwise gate driver drives the gate voltage  $v_{G1}$  with nine steps. The stepwise switch drivers generate the staggered pulses that drive the switches  $S_R/S_F$  in the stepwise gate driver to create the stepwise waveform for  $v_{G1}$ .

The delay line circuits provide the edges that set the timing for the pulsed outputs of the stepwise switch controllers. In addition to providing the stepwise timing signals, the slow delay line sets the switching frequency and on-time for  $M_1$ . An output of the slow delay line feeds back to the *reset* input of the slow delay line, making an oscillator that sets the DC-DC converter switching frequency. A mux selects which delay line output is used for the switching frequency, allowing 64 different switching frequencies ranging from 350 Hz to 0.6 Hz, externally programmable with the 6-bit *frequency set*. The chosen frequency sets the input impedance of the DC-DC converter, ranging from 1  $\Omega$  to 600  $\Omega$ . A 65<sup>th</sup> output from the slow delay line is selected when the DC-DC converter enters the *hibernate* state, lowering the switching frequency to 0.2 Hz.

The secondary power FETs  $M_{2P}$  and  $M_{2N}$  are used as active rectifiers with zero-current-switching. The  $V_{IN}$  detect circuits compare the time that secondary power FETs  $M_{2P}$  and  $M_{2N}$  are conducting against a reference delay that is generated by the fast delay line. This is used to detect whether  $|V_{IN}|$  is less than 0.5 mV. When  $|V_{IN}|$  is detected to be less than 0.5 mV, the converter is put into the *hibernate* state.

A voltage monitor circuit provides a *power good* signal like in [20] that goes high when  $V_{OUT}$  has charged above 2.7 V and it stays high until  $V_{OUT}$  drops below 2.5 V. It operates at a very low duty cycle when *power good* is low to conserve. Switching of  $M_1$  is stopped when  $V_{OUT} > 2.8\text{ V}$  to avoid excessive voltages.

## III. STEPWISE GATE-DRIVE

For very low input voltages, the gate-drive of the primary power FET  $M_1$  dominates the losses [2],[3] so reducing those losses allows the DC-DC converter to operate efficiently at lower input voltages. A common approach to reducing these losses is to use a deep submicron CMOS technology with very low FET gate capacitance for a given channel resistance. However, such processes have high leakage currents that result in high static power consumption [21]. Therefore, a low-leakage 600-nm process is used and the gate of  $M_1$  is driven

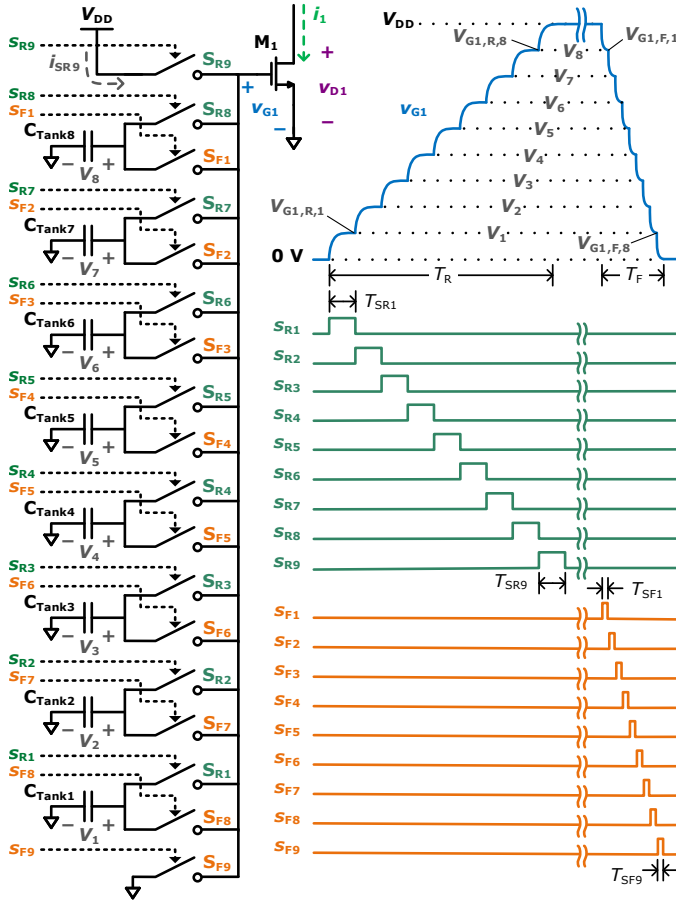


Fig. 3. Stepwise gate driver and waveforms for one switching cycle.

with an adiabatic driver to reduce gate-drive energy. One option would be an inductive resonant gate driver such as in [22], but implementing quality inductors on-chip can be impractical. Alternatively, this paper proposes using the inductor-less stepwise charging technique introduced in [23] and [24] to reduce the gate-drive losses. Stepwise charging has been utilized to reduce power in ADCs [25], [26], clock drivers [27], touch sensors [28], and switched-capacitor DC-DC converters [29] but until now use in inductive DC-DC converters has only been theorized [17] and has not been demonstrated in hardware.

Fig. 3 shows the proposed stepwise gate-drive circuit. Eight capacitors hold charge at approximately equal steps between 0 V and  $V_{DD}$ . To turn on power FET  $M_1$ , switches  $S_{R1}$  through  $S_{R9}$  (implemented as NMOS devices) are turned on then off sequentially and individually. This creates a step pattern for the  $M_1$  gate voltage  $v_{G1}$  as it approaches the supply voltage  $V_{DD}$ . To turn  $M_1$  off, switches  $S_{F1}$  through  $S_{F9}$  are turned on then off sequentially and individually, stepping the voltage down to 0 V. Under steady-state, where  $v_{G1}$  has completed several step-up/step-down cycles, the average voltage across each  $C_{Tank}$  capacitor becomes evenly distributed between 0 V and  $V_{DD}$  [24]. Energy is only drawn from the power supply  $V_{DD}$  on the final rising step, so the energy to drive the gate becomes

$$E_{\text{Gate-Drive}} \approx C_{\text{Gate}} V_{DD} (V_{DD} - V_{N-1}), \quad (1)$$

where  $C_{\text{Gate}}$  is the gate capacitance of  $M_1$  that is being driven, and  $N$  is the number of voltage steps. In the proposed circuit  $N = 9$ . In steady-state the average voltage across each capacitor is ideally uniformly distributed so (1) can be re-written as

$$E_{\text{Gate-Drive}} \approx C_{\text{Gate}} V_{DD} \left( V_{DD} - V_{DD} \frac{N-1}{N} \right), \quad (2)$$

$$E_{\text{Gate-Drive}} \approx C_{\text{Gate}} \frac{V_{DD}^2}{N}. \quad (3)$$

In the case of a conventional gate driver,  $N = 1$ .

#### A. Stepwise Gate Driver Efficiency

Equation (3) assumes  $S_R$  and  $S_F$  are ideal switches while also assuming  $C_{\text{Tank}} \gg C_{\text{Gate}}$ . If each step is not given enough time to settle, then the step will not fully reach the corresponding  $C_{\text{Tank},k}$  capacitor voltage  $V_k$ . Also, the voltages  $V_k$  will have ripple as charge is transferred between  $C_{\text{Tank}}$  and  $C_{\text{Gate}}$ , causing each step to settle short of  $V_k$  even if sufficient settling time is provided. Svensson [24] and Dancy [17] attempt to model these non-idealities but do not accurately model the effects of step settling time. Park [28] sets up equations for an accurate analytical model but stops short of a final closed-form solution. Using principles similar to those used in [28] and [30], a model for stepwise gate driver energy that accurately takes into account finite  $C_{\text{Tank}}$  and finite settling time was developed.

Switches  $S_R$  and  $S_F$  have an on-state resistance of  $R_{SR}/R_{SF}$  and an on-time of  $T_{SR}$  and  $T_{SF}$  for each step. Each step follows an RC charging behavior where the “C” is the series combination of  $C_{\text{Tank}}$  and  $C_{\text{Gate}}$ :

$$C_{\text{Series}} = \frac{C_{\text{Tank}} C_{\text{Gate}}}{C_{\text{Tank}} + C_{\text{Gate}}}. \quad (4)$$

The percentage that each step  $V_{G1,R,k}$  reaches the voltage  $V_k$  is defined as  $r$  (for rising steps) and  $f$  (for falling steps) such that

$$r := \frac{V_{G1,R,k} - V_{G1,R,k-1}}{V_k - V_{G1,R,k-1}}, \quad (5)$$

$$f := \frac{V_{G1,F,k} - V_{G1,F,k-1}}{V_{N-k} - V_{G1,F,k-1}}, \quad (6)$$

$$r = \frac{2C_{\text{Series}}}{C_{\text{Series}} + C_{\text{Gate}} \coth\left(\frac{T_{SR}}{2R_{SR}C_{\text{Series}}}\right)}, \quad (7)$$

$$f = \frac{2C_{\text{Series}}}{C_{\text{Series}} + C_{\text{Gate}} \coth\left(\frac{T_{SF}}{2R_{SF}C_{\text{Series}}}\right)}. \quad (8)$$

For an ideal stepwise driver,  $r = f = 1$ . Since  $C_{\text{Tank}}$  voltages have ripple,  $V_k$  is defined as the average of that voltage (not the average across time, but the average of the final voltage after a rising step and the final voltage after a falling step).

The analysis makes some underlying assumptions: the final rising step is allowed to fully settle to  $V_{DD}$ , the final falling step is allowed to fully settle to 0 V,  $r$  for all other rising steps are equal, and  $f$  for all other falling steps are equal.<sup>1</sup> With those assumptions, the value of  $v_{G1}$  at the end of each rising step was calculated to be

$$V_{G1,R,k} = \begin{cases} \sum_{i=1}^k r(1-r)^{k-i} V_i, & 0 < k < N \\ V_{DD}, & k = N \end{cases}, \quad (9)$$

<sup>1</sup> Fig. 3, shows  $T_{SR9}$  and  $T_{SF9}$  to violate the assumptions by being relatively short, however switch resistance was set low enough such that  $v_{G1}$  still settles very close to  $V_{DD}/0$  V. All  $T_{SR}$  and all  $T_{SF}$  were given similar duration for simplicity.

such that  $k = 1$  is the first step, and  $V_{G1,R,k} = V_k$  if  $r = 1$ . The voltage at the end of each falling step was calculated to be

$$V_{G1,F,k} = V_{DD}(1-f)^k + \sum_{i=0}^{k-1} f(1-f)^i V_{N-k+i} \quad (10)$$

for  $0 < k < N$ , and for the last falling step  $V_{G1,F,N} = 0$  V.

When  $r < 1$  or  $f < 1$ , the voltages  $V_k$  across each  $C_{\text{Tank}}$  are no longer uniformly distributed as in the ideal case. In steady-state, the charge leaving a  $C_{\text{Tank}}$  capacitor at the rising step must equal the charge entering that capacitor at the falling step. Therefore, the  $v_{G1}$  step size going into a given  $C_{\text{Tank}}$  must equal for rising and falling edges, giving the following relationship:

$$V_{G1,F,k} = \begin{cases} V_{DD} + V_{G1,R,N-2} - V_{G1,R,N-1}, & k = 1 \\ V_{G1,F,k-1} + V_{G1,R,N-k-1} - V_{G1,R,N-k}, & k > 1 \end{cases} \quad (11)$$

Combining (9)–(11) produces a matrix equation that can solve for  $V_k$ . The matrix follows a predictable pattern. In the case of  $N = 5$ , the matrix equation is

$$\begin{bmatrix} r^2(1-r)^2 & r^2(1-r) & r^2 & -r-f \\ r^2(1-r) & r^2 & -r-f & f^2 \\ r^2 & -r-f & f^2 & f^2(1-f) \\ -r-f & f^2 & f^2(1-f) & f^2(1-f)^2 \end{bmatrix} \begin{bmatrix} V_1 \\ V_2 \\ V_3 \\ V_4 \end{bmatrix} = \begin{bmatrix} -fV_{DD} \\ -f(1-f)V_{DD} \\ -f(1-f)^2V_{DD} \\ -f(1-f)^3V_{DD} \end{bmatrix} \quad (12)$$

Finally, the gate-drive energy can be calculated:

$$E_{\text{Gate-Drive}} = C_{\text{Gate}} V_{DD} (V_{DD} - V_{G1,R,N-1}), \quad (13)$$

where  $V_{G1,R,N-1}$  is a solution to (9). A more detailed derivation is available in [31].

Fig. 4 shows how the settling time  $T_{SF}$  affects  $E_{\text{Gate-Drive}}$  for various values of  $N$  and  $C_{\text{Tank}} / C_{\text{Gate}}$ . For the proposed DC-DC converter, the  $v_{G1}$  risetime  $T_R$  can be much longer than the falltime  $T_F$  (for reasons that will be explained in Section IV.A.) and therefore rising steps are assumed to fully settle such that  $T_{SR} \gg R_{SR}C_{\text{Series}}$ . Gate-drive energy is normalized to that of a conventional gate driver.  $T_{SF}$  is normalized to  $R_{SF}C_{\text{Gate}}$  (not the settling time constant, which is  $R_{SF}C_{\text{Series}}$ ). Calculated results (dotted lines) are compared to those of simulation (solid lines) to show the accuracy of the model.

One final consideration in the efficiency of stepwise gate-drive is the energy required to drive the switches  $S_R$  and  $S_F$ . There is a quality factor  $\rho$  that determines how much energy is consumed by turning on a switch that has a given resistance:

$$E_{SR,k} = \frac{\rho_{R,k}}{R_{SR,k}}, \quad E_{SF,k} = \frac{\rho_{F,k}}{R_{SF,k}}, \quad (14)$$

where  $\rho$  can be determined empirically in simulation and the value is dependent on the parameters of the NMOS device that makes the switch and the design of the circuitry that drives the switch. The value of  $\rho$  will be different for each switch due to varying NMOS gate-to-source and source-to-body voltages, but for the purpose of circuit optimization an average value can be used so that the total energy to drive the stepwise switches is

$$E_{\text{Switch-Drive}} = NE_{SR} + NE_{SF}. \quad (15)$$

The total energy consumed by driving the gate then becomes

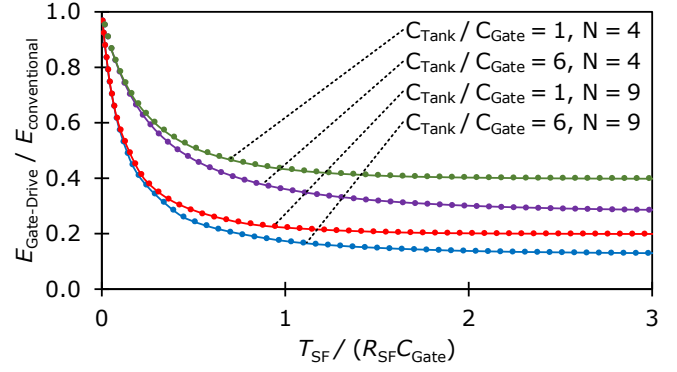


Fig. 4. Simulated (solid lines) and calculated (dotted lines) effect of falling-edge step settling time on an otherwise ideal stepwise gate driver's efficiency for various  $C_{\text{Tank}} / C_{\text{Gate}}$  ratios and step counts  $N$ .

the sum of  $E_{\text{Gate-Drive}} + E_{\text{Switch-Drive}}$ , which will be discussed in Section VIII about optimizing the stepwise gate driver.

### B. Stepwise Switch Driver

The stepwise switch driver, shown in Fig. 5, provides staggered pulses  $s_R$  and  $s_F$  to drive the switches  $S_R$  and  $S_F$  in the stepwise gate driver. Svensson [23] uses complimentary NMOS and PMOS devices for the switches. The problem with that architecture is that the switches connected to the  $V_k$  voltages near  $V_{DD} / 2$  will not turn on when  $V_{DD}$  is less than the combined threshold voltages of the PMOS and NMOS. To address that deficiency, the proposed circuit uses only NMOS devices for  $S_R$  and  $S_F$ , driven with a voltage doubler similar to that in [32] to provide sufficient voltage to fully turn on the NMOS devices. This allows the circuit to operate down to  $V_{OUT} = V_{DD} = 1.5$  V, even though the NMOS threshold voltage is 1.0 V. The circuit was fabricated in a CMOS process rated for 5.5 V, so the doubled voltage does not exceed the voltage ratings when  $V_{OUT} = V_{DD} = 2.7$  V. If voltage ratings were a problem, then the circuit in [33] could be used to drive  $S_R/S_F$ .

### C. Stepwise Timing Control

The stepwise switch driver in Fig. 5 requires consecutive timing signals,  $y_n$ , to generate the staggered stepwise switching signals  $s_R$  and  $s_F$ . The timing circuit in [23] uses a finite state machine to produce the timing signals, which requires a clock and substantial logic, while [29] utilizes the inherent delay of current-starved logic gates. The proposed approach is to use the delay line circuit included in Fig. 5. Two of these delay line circuits are used: a “slow” delay line generates the timing for the rising edge of  $v_{G1}$  and a “fast” delay line generates the timing for the faster falling edge. In the delay line circuits, many series PMOS devices share a common gate bias voltage  $V_{SG}$ , which is set by a bias generator consisting of a gate-to-drain connected PMOS device and a resistor  $R_B$ . The bias generator operates at a low duty cycle to save power and  $V_{SG}$  is held with a capacitor  $C_B$  while the bias generator is disabled.

At reset, every  $dly$  node is pulled low. Once reset is low, the first  $dly$  is released and rises. Once the first  $dly$  rises to near  $V_{DD}$ , the next  $dly$  starts to rise, thereby producing a series of successive rising edges. Each successive  $dly$  signal does not start to rise until the previous  $dly$  is near  $V_{DD}$  due to the corresponding PMOS transistor being in the cutoff region. The time it takes each  $dly$  node to rise from 0 V to near  $V_{DD}$  is determined by the effective total intrinsic capacitance  $C_{dly}$  on



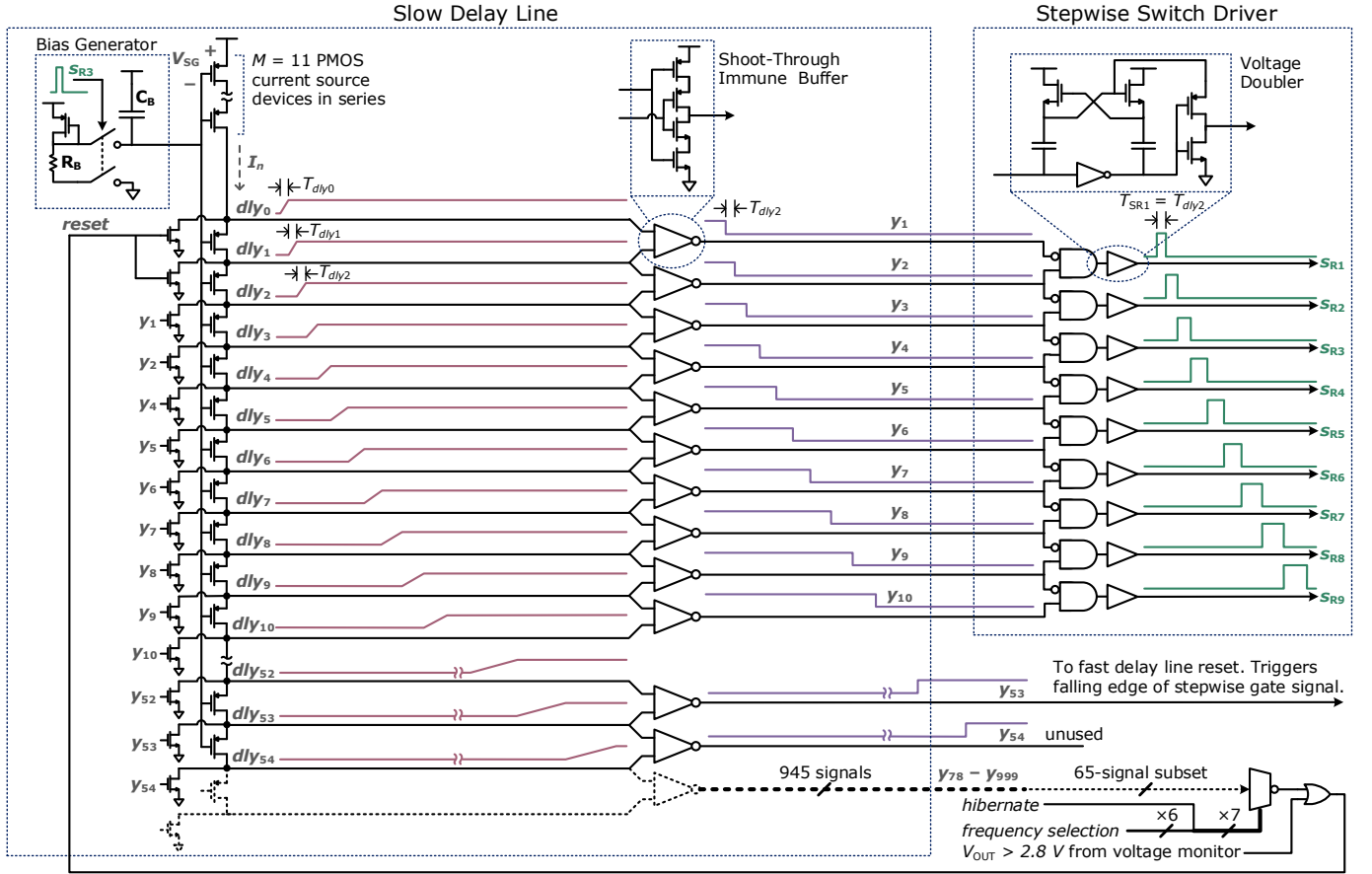


Fig. 5. Stepwise control circuit for the rising edge of the stepwise gate signal, including the slow delay line and the stepwise switch driver. The circuit generating the falling edge of the stepwise gate voltage uses the fast delay line with a similar architecture.

each  $dly$  node and the charging current  $I_n$  sourced by the PMOS current sources:

$$T_{dly,n} = C_{dly} \frac{V_{DD} - (V_{SG} - V_{TH})}{I_{dly,n}}, \quad (16)$$

where  $V_{TH}$  is the PMOS threshold voltage and a positive number. As each successive  $dly$  node voltage rises, the corresponding PMOS connected to that node effectively becomes an additional device in the series PMOS current source chain, resulting in the charging current  $I_{dly,n}$  to be slightly less for each successive  $dly$ :

$$I_{dly,n} \approx \frac{V_{DD} - V_{SG}}{R_B} \frac{K}{(M + n)}, \quad (17)$$

with  $M = 11$  being the number of series PMOS devices without a  $dly$  node on the source and  $K$  being the ratio of the W/L ratios between a “ $dly$ ” PMOS device and the PMOS device in the bias generator. Equation (17) only holds if  $V_{SG}$  is constant, and for small  $n$  it practically is. However, capacitive coupling causes  $V_{SG}$  to reduce slightly each time a  $dly$  node voltage rises and this becomes significant for large  $n$ , resulting in an additional reduction in each  $I_{dly,n}$ . Per the charge-sharing equation, the amount that  $V_{SG}$  reduces by for each successive  $dly$  is

$$\Delta V_{SG} = \frac{C_{GS} + C_{GD}}{C_B + (C_{GS} + C_{GD})N_{dly}}, \quad (18)$$

where  $C_{GS}$  and  $C_{GD}$  are the gate-to-source and gate-to-drain capacitance of each “ $dly$  PMOS” respectively and  $N_{dly} = 1000$

is the total number of  $dly$  nodes.  $\Delta V_{SG}$  was determined in simulation to be 0.13 mV. At  $n = 0$ ,  $V_{SG} - V_{TH} = 64$  mV, which is low enough to be considered subthreshold operation. Using the subthreshold current formula from [34] (omitting channel-length modulation), the charging current becomes

$$I_{dly,n} = I_0 \frac{M}{M + n} e^{\left(1 - \frac{V_{SG0} - n\Delta V_{SG} - V_{TH}}{\alpha V_T}\right)^2}, \quad (19)$$

where  $I_0 = 8.8$  nA and  $V_{SG0} = 1.10$  V are the current and gate-to-source voltage before any  $dly$  node rises (at  $n = 0$ ).  $V_T = 25$  mV is the thermal voltage and  $\alpha$  (referred to as  $n$  in [34]) was determined empirically in simulation to be 2.2. Another factor that can affect the  $I_{dly,n}$  current is the static leakage on each  $dly$  node. Simulation showed that under typical conditions the leakage is negligible, but under hot temperatures or very large  $N_{dly}$  leakage can have a significant effect on  $T_{dly}$ , even preventing  $dly$  transitions altogether.

Fig. 6 shows the simulated waveforms of the slow delay line. Fig. 7 shows the time between  $dly$  signals  $T_{dly,n}$  as determined from equations (16), (18), (19), simulation, and measurement of the silicon. Simulated and calculated results match closely with the measured results up to  $n = 300$ , where the measured delays start to deviate from the predicted values. This difference could be attributed to unmodelled leakage current on the  $dly$  nodes or from inaccurate modelling of the subthreshold behavior of the PMOS devices. There is a gap in the silicon measured data between  $n = 10$  and  $n = 90$  due to a lack of visibility into the circuit.

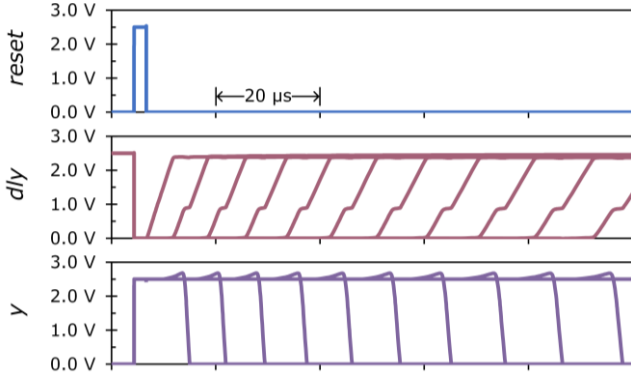


Fig. 6. Simulated waveforms of the slow delay line.

The slow edge rates of the  $dly$  signals would result in shoot-through currents in the downstream logic. An inverting buffer that is immune to shoot-through currents prevents this by using two NMOS and PMOS pairs, which are switched in a staggered fashion. The output of the shoot-through immune buffer is briefly undriven during the time after the first input has transitioned and before the second input has transitioned, so special care was taken in layout to prevent parasitic capacitive coupling from causing the output of the buffer to drift low during this time.

It is clear from Fig. 7 that each successive  $T_{dly,n}$  is slower than the previous. This behavior is not ideal for the stepwise gate driver but is useful for generating very slow timing signals when many stages are used, making the slow delay line useful for controlling the on-time and switching period of the DC-DC converter primary power FET  $M_1$ , and replacing the need for more timing circuits. The 53<sup>rd</sup> output  $y_{53}$  triggers the falling edge of the stepwise gate signal (controlled by the fast delay line), setting the duration in which power FET  $M_1$  is on:  $T_{i1,rise}$ . One of 65 delay outputs is selected through a mux and is fed back to the *reset* signal to set the oscillation frequency (the switching frequency of  $M_1$ ). The selectable switching frequency enables the input impedance to be programmed to match with the TEG for maximum power extraction, or “MPPT” as described in [4]–[6],[35],[36] (this is opposed to the “OCV” MPPT method described in [37]). When the *hibernate* input is high, the final delay output  $y_{999}$  is used, setting the frequency to 0.2 Hz to minimize quiescent power consumption.

#### IV. DC-DC TOPOLOGY CONSIDERATIONS

There are many DC-DC topologies that can be used to step up a voltage. One option would be a switched capacitor circuit such as in [38], but using a switched capacitor circuit to step up a voltage from 1 mV to 2.5 V would require a large number of conversion stages. An inductive architecture can theoretically achieve any step-up ratio in just one conversion stage. The simplest form of inductive architecture is a single-inductor boost converter as in [2]. The two main problems with the single-inductor boost converter are poor efficiency for very low input voltages and difficulty supporting bipolar inputs. These two problems are solved by using a flyback converter topology.

##### A. Efficiency Considerations

For very low  $V_{IN}$ , the conversion losses in a boost converter are dominated by the resistance, gate capacitance, and drain capacitance of  $M_1$  [2]. The resistance of  $M_1$  can be reduced by

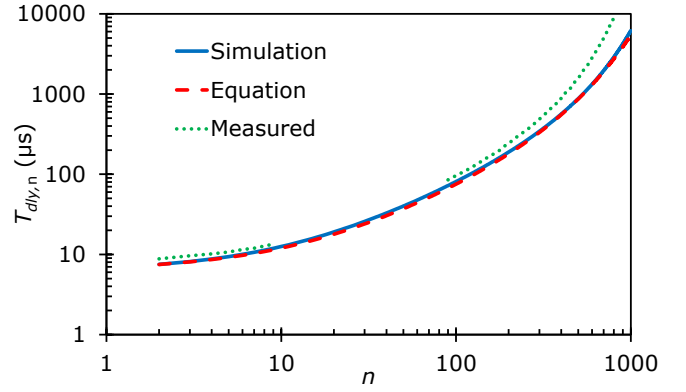


Fig. 7. Time between  $dly$  signals,  $T_{dly,n}$ , vs.  $n$  as determined by simulation, equations (16), (18), (19), and measurement of the silicon.

increasing the channel width at the expense of higher capacitive losses. The losses due to gate capacitance can then be reduced by using stepwise gate drive. However, losses due to drain capacitance are difficult to address using a simple boost topology since the drain node  $v_{D1}$  must charge from 0 V to  $V_{OUT}$  for each cycle. Zero-voltage-switching (ZVS) techniques [39] reduce these losses, but only to an extent. If the energy required to charge the drain node capacitance exceeds the energy stored in the inductor, then  $v_{D1}$  will not be able to charge up to  $V_{OUT}$  and no current would flow to the output. The energy required to charge the drain node capacitance on a boost converter is

$$E_{C,D1} = \frac{1}{2} C_{D1} \hat{V}_{D1}^2, \quad (20)$$

where  $C_{D1}$  is the total capacitance on the drain node and  $\hat{V}_{D1}$  is the peak voltage of  $v_{D1}$ . For a boost converter,  $\hat{V}_{D1} = V_{OUT}$ .

Another source of losses in a boost converter is the energy consumed during the transition of  $M_1$  from the “on” state to the “off” state—referred to here as “transition losses”. These losses are only significant when the falling edge of gate voltage  $v_{G1}$  is slow, such as when stepwise gate drive is used. If  $v_{G1}$  transitions from  $V_{DD}$  to 0 V before  $v_{D1}$  has risen significantly, then there is little power lost. If  $v_{G1}$  transitions slowly, then  $M_1$  will spend time in a region of operation where the channel current is low enough such that the drain voltage  $v_{D1}$  is rising, but current is still being conducted through the channel—causing transition losses [40]. These transition losses are separate from the energy that gets stored in the power FET drain capacitance. To calculate the transition losses from simulation data, the power  $p_1$  flowing into the drain of  $M_1$  is integrated across the time that the transition occurs. Then the portion of that energy that goes into charging the drain capacitance and the energy associated with standard conduction losses are subtracted out. The energy that remains are the transition losses:

$$E_{\text{Tran-Loss}} = \int_{T_1}^{T_3} p_1 dt - E_{C,D1} - \hat{I}_1^2 R_{on1} (T_2 - T_1), \quad (21)$$

where

$$p_1 = i_1 v_{D1}, \quad (22)$$

$i_1$  is the current through  $M_1$ ,  $\hat{I}_1$  is the peak value of  $i_1$ , and  $R_{on1}$  is the resistance of the channel of  $M_1$  while  $v_{G1}$  is highest.  $T_1$  and  $T_3$  are the times that  $v_{G1}$  starts and ends the transition from high to low ( $T_3 - T_1 = T_F$ ).  $T_2$  is the time that  $v_{G1}$  crosses the threshold voltage of  $M_1$ , where the channel current becomes

effectively zero. Transition losses during the rising edge of  $v_{G1}$  are generally negligible for a converter operating in DCM because, at  $M_1$  turn-on,  $i_1$  is initially zero and ramps up slowly due to inductance. Transition losses at turn-on would only be significant if the  $v_{G1}$  risetime  $T_R$  was comparable to that of the inductor current risetime  $T_{i1,rise}$ . Therefore,  $T_R$  can be much longer than  $T_F$ .

To address the drain capacitance losses and transition losses associated with a boost converter, a flyback topology is used. By using a flyback transformer in place of a single inductor, the peak  $\hat{V}_{D1}$  of the drain voltage  $v_{D1}$  can be reduced by the turns ratio  $N_t$  of the flyback transformer:

$$\hat{V}_{D1} = V_{IN} + \frac{V_{OUT}}{N_t}. \quad (23)$$

This in turn reduces the energy required to charge the drain node capacitance per (20) and the transition losses per (21), (22), (23). To illustrate the transition losses, Fig. 8 shows the current, voltage, and power waveforms for  $M_1$  during a very slow  $v_{G1}$  high-to-low transition. It shows that the power  $p_1$  flowing into  $M_1$  with a 1:2 flyback transformer is lower compared to a boost converter, while a 1:1 flyback transformer does not provide the same benefit. A higher flyback transformer turns ratio reduces transition losses caused by a slow  $v_{G1}$  slew rate. Fig. 9 shows the simulated relationship between transition losses and the time  $v_{G1}$  takes to transition from 2.5 V to 0 V. In this simulation,  $v_{G1}$  was transitioned linearly rather than in a stepwise fashion.

Using a flyback topology does introduce a new switching node  $v_{D2}$  that still must swing from 0 V to  $V_{OUT}$ , but in the proposed DC-DC converter the capacitance on node  $v_{D2}$  is much less than the capacitance on  $v_{D1}$ . This is because the transformer secondary current  $i_2$  is much lower than the primary current  $i_1$  and the duration that  $i_2$  flows ( $T_{i2,fall}$ ) is less than the duration that  $i_1$  flows ( $T_{i1,rise}$ ). So, the rectifier device can be much smaller than  $M_1$ , with much higher resistance and lower capacitance.

### B. Supporting a Bipolar Input

Since a TEG can produce either positive or negative voltages, the DC-DC converter must support input voltages of either polarity. Alhawari [6] addresses this for a boost converter

by using an H-bridge switch network to reverse the polarity when needed, while [19] uses a boost-flyback hybrid technique where the DC-DC converter acts as a single-coil boost converter for one polarity and as a flyback converter for the opposite polarity. For the proposed application, an H-bridge switch network as in [6] would require an extremely large amount of die area to keep the parasitic resistance of the H-bridge less than that of  $M_1$ . The boost-flyback hybrid method of [19] operates similar to a single-inductor boost converter for positive  $V_{IN}$ , so it cannot take full advantage of the benefits of a flyback transformer. Bipolar implementations in [18] and [20] require two transformers. The bipolar converter in [16] uses just one transformer but the implementation is undisclosed.

The proposed solution to bipolar input voltage uses one flyback transformer with two secondary windings (or a single center-tapped secondary winding), shown in Fig. 10. Each secondary winding is dedicated to one input voltage polarity and each has its own rectifier. The rectifier devices can have much higher resistance than  $M_1$  due to conducting less current and for a shorter period of time. Therefore,  $M_1$  dominates the active area of the chip (not including  $C_{Tank}$ ).

This method of supporting bipolar inputs has two considerations. First, the method only works when the voltage  $v_{D1}$  does not exceed the turn-on voltage of the  $M_1$  body diode:

$$v_{D1} > -V_{Diode}. \quad (24)$$

Rewriting in terms of  $V_{IN}$  and  $V_{OUT}$  yields

$$V_{IN} - \frac{V_{OUT}}{N_t} > -V_{Diode}. \quad (25)$$

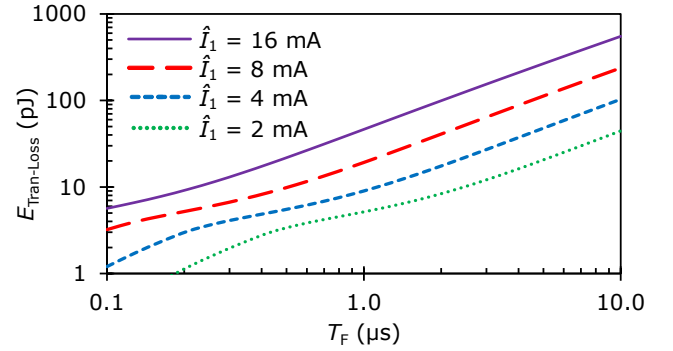


Fig. 9. Simulated  $M_1$  transition losses vs. gate voltage transition time  $T_F$ .

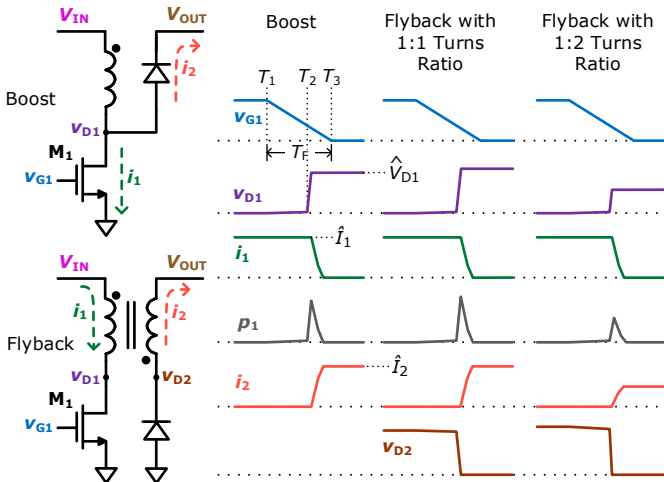


Fig. 8. Demonstrating the reduced transition losses when using a flyback converter.

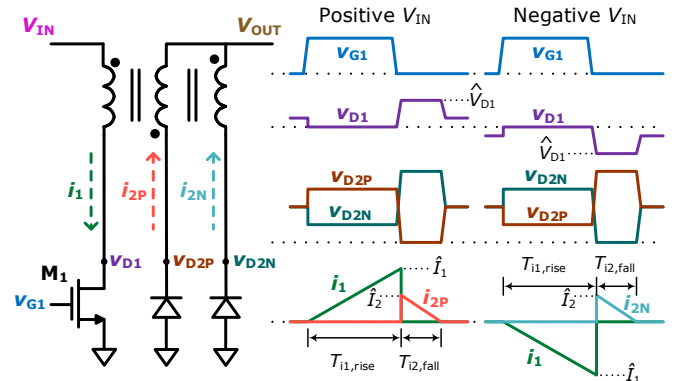


Fig. 10. Using a flyback transformer with two anti-parallel secondary windings supports a bipolar input. The turns ratio in this illustration is 1:2:2.

This limitation only applies to negative  $V_{IN}$  and is mitigated by a large transformer turns ratio  $N_t$ .

The second consideration is that if either voltage  $v_{D2P}/v_{D2N}$  goes significantly below 0 V while  $M_1$  is conducting (due to large  $V_{IN}$ ) then the rectifier diode will conduct and the DC-DC converter will behave like a forward converter as in [41]. Consequently, the inductance of the primary winding will stop limiting the input current and  $i_1$  will increase drastically. This effectively clamps  $V_{IN}$  such that

$$|V_{IN}| < \frac{V_{OUT}}{N_t}. \quad (26)$$

The clamping effect is not catastrophic, but it decreases the DC-DC converter's input impedance, affecting maximum power transfer from the TEG. In this work, the transformer turns ratio was set to  $N_t = 20$ , avoiding clamping at  $V_{IN} = 50$  mV.

### V. ACTIVE RECTIFICATION

The DC-DC converter operates in DCM and requires a form of rectification to allow current to flow to the output while preventing current from flowing from the output back into the converter. A diode like those shown in Fig. 8 and Fig. 10 is the simplest implementation but is inefficient due to the large forward voltage drop. Replacing the diodes with MOSFETs reduces the voltage drop significantly when switched at the appropriate times. Switching the MOSFET off as the current crosses 0 A is referred to as zero-current-switching (ZCS). To achieve ZCS, this work uses a modified version of the feedback technique that was introduced in [42] and later adapted in [2], followed by [4],[5],[19],[43] for low  $V_{IN}$  DC-DC converters.

Fig. 11 shows the proposed active rectifier implementation. The rectifier device  $M_2$  is switched on when the polarity of the drain voltage  $v_{D2}$  becomes negative (ZVS) and off when  $v_{D2}$  goes positive (ZCS). A comparator is used to detect this

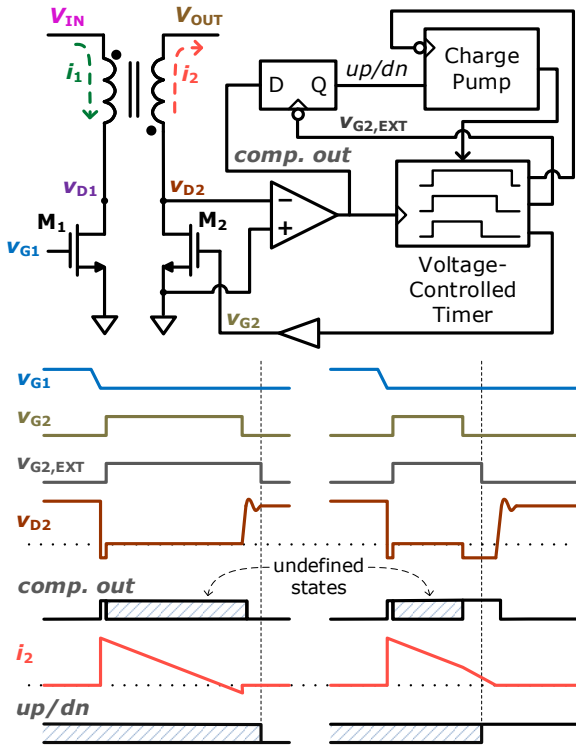


Fig. 11. Active rectifier circuit for zero-current-switching.

polarity. However, when  $M_2$  is in the “on” state the voltage drop is very small, making it difficult to accurately sense the polarity. To avoid this problem, the polarity of  $v_{D2}$  is only sampled while  $M_2$  is in the “off” state. For turn-on,  $M_2$  already starts in the “off” state, so the comparator directly controls when  $M_2$  is switched on. But for turn-off, an adaptive timing method is used. A voltage-controlled timer sets the on-time of  $M_2$ . The polarity of  $v_{D2}$  is sampled *after*  $M_2$  turns off and the duration of the on-time for the next cycle is adjusted based on when the polarity reversed. If the polarity reversed after  $M_2$  turned off—plus a short delay—then the on-time is increased for the next cycle. Otherwise, the on-time is decreased. Since  $M_2$  is much smaller than  $M_1$  it is driven with a conventional gate driver and stepwise gate-drive not needed.

### VI. INPUT VOLTAGE DETECTION

When  $|V_{IN}|$  is too low, the input energy per cycle  $E_{IN}$  is less than the energy consumed by losses (efficiency becomes less than 0%). Running the DC-DC converter at the normal operating frequency would quickly discharge the output storage capacitors due to the quiescent power consumption. Desai [44] proposes hibernating the converter when  $V_{IN}$  is so low that  $v_{D1}$  does not transition high enough to deliver any current to the output, but that is less than the 0% efficiency threshold. With that approach the converter could be wasting power with negative efficiency while  $V_{IN}$  is barely high enough to cause  $v_{D1}$  transitions but not delivering power to the output. The proposed approach is to hibernate precisely when the efficiency is below 0%. In the proposed DC-DC converter, that typically occurs when  $|V_{IN}| < 0.5$  mV. Sensing  $V_{IN}$  directly is impractical due to the required measurement accuracy. Instead,  $V_{IN}$  is measured indirectly through timing as proposed in [5],[2] and illustrated in Fig. 12. Ignoring parasitics, the relationship is

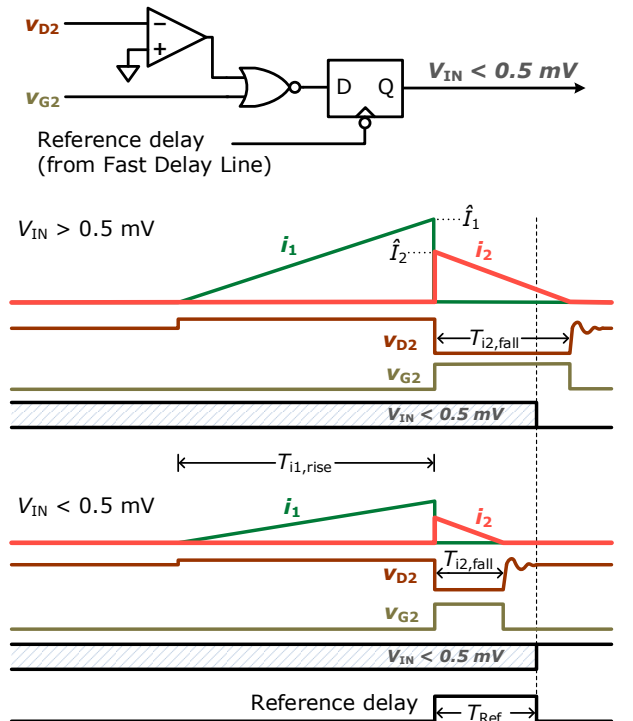


Fig. 12. Input voltage detection.



$$V_{IN} \approx \frac{V_{OUT}}{N_t} \cdot \frac{T_{i2,fall}}{T_{i1,rise}}, \quad (27)$$

where  $N_t$  is the transformer turns ratio. By comparing  $T_{i1,fall}$  to a pre-programmed reference delay  $T_{Ref}$ ,  $V_{IN}$  can be estimated and compared to a threshold  $V_{IN,Th}$  (0.5 mV) such that

$$V_{IN,Th} \approx \frac{V_{OUT}}{N_t} \cdot \frac{T_{i2,fall}}{T_{Ref}}. \quad (28)$$

Equation (28) shows that  $V_{IN,Th}$  is proportional to  $V_{OUT}$ . This relationship is desirable for setting the hibernation threshold voltage because the minimum  $V_{IN}$  ( $V_{IN}$  where the efficiency is 0%) is also approximately proportional to  $V_{OUT}$ . If  $T_{i1,rise}$ , and  $T_{Ref}$  were fixed, then the  $V_{IN}$  threshold would inherently track the 0% efficiency point. In this work,  $T_{i1,rise}$  and  $T_{Ref}$  are sensitive to  $V_{OUT}$  due to the delay line design, so the hibernation threshold does not track the 0% efficiency point as well as it would if the timing were better controlled.

## VII. OUTPUT VOLTAGE MONITOR

A voltage monitor circuit in Fig. 13 was implemented to inform the load when the output voltage is above 2.5 V and the power supply is at a good level, similar to the *power good* function in [20]. This function is achieved by comparing a divided version of  $V_{OUT}$  with a reference voltage generated by a bandgap circuit. Hysteresis is achieved by adjusting the divide ratio, so *power good* transitions high when  $V_{OUT} > 2.7$  V and low when  $V_{OUT} < 2.5$  V.

To minimize power consumption when *power good* is low, the comparator and bandgap circuit are enabled only while  $y_5$  from the slow delay line is high and only once every 32 cycles. When *power good* is high it is assumed that the load current will overshadow the 4  $\mu$ A current consumption of the comparator and bandgap, so the comparator and bandgap are left on.

The voltage monitor also keeps the DC-DC converter from allowing  $V_{OUT}$  to charge above 2.8 V. If *power good* is high and the slow delay line is in the *reset* state, the comparator threshold is set to 2.8 V. If  $V_{OUT} > 2.8$  V then the slow delay line is kept in *reset*—preventing further DC-DC converter switching—until the comparator output transitions low.

## VIII. EFFICIENCY OPTIMIZATION

To maximize DC-DC converter efficiency, the following parameters were optimized:  $M_1$  on-resistance  $R_{on1}$  from sizing,  $M_1$  on-time  $T_{i1,rise}$ , and stepwise parameters  $N$ ,  $R_{SF}$ , and  $T_F$  were optimized.  $T_{i1,rise}$  was set to 1.3 ms to maximize the energy transferred per cycle. A higher on-time would cause transformer saturation at  $V_{IN} = 50$  mV. The  $R_{on1}$  was chosen to balance gate-drive and  $E_{C,D1}$  losses with conduction losses  $E_{M1,cond}$  at  $V_{IN} = 1$  mV and  $V_{OUT} = 2.5$  V while taking into account the energy savings of stepwise gate-drive:

$$E_{Gate-Drive} + E_{Switch-Drive} + E_{C,D1} = E_{M1,cond}, \quad (29)$$

where,

$$E_{M1,cond} = \frac{1}{3} \hat{I}_1^2 R_{on1} T_{i1,rise}. \quad (30)$$

The stepwise gate driver was optimized by minimizing the net losses  $E_{SW,net}$  that are sensitive to stepwise driver design parameters  $N$ ,  $R_{SF}$ , and  $T_F$ :

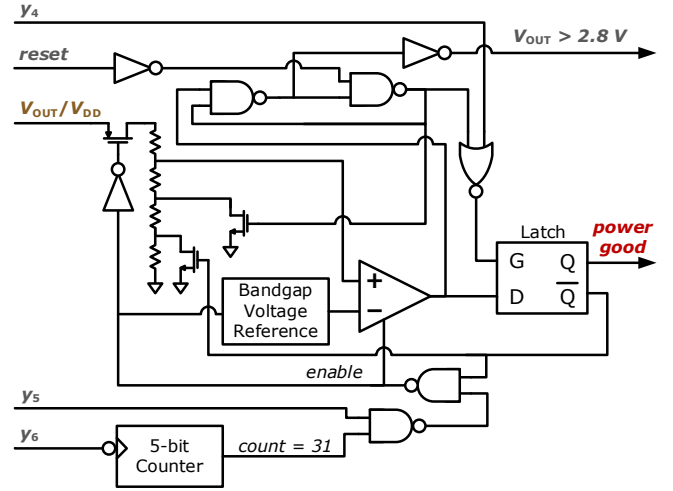


Fig. 13. Voltage monitor circuit.

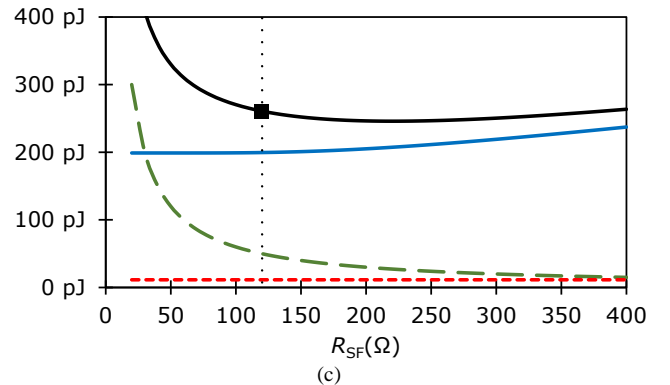
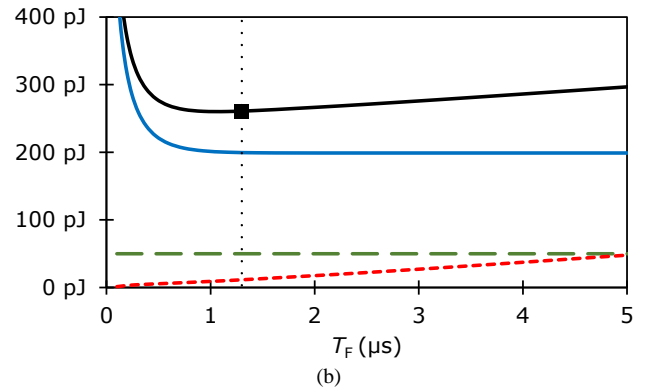
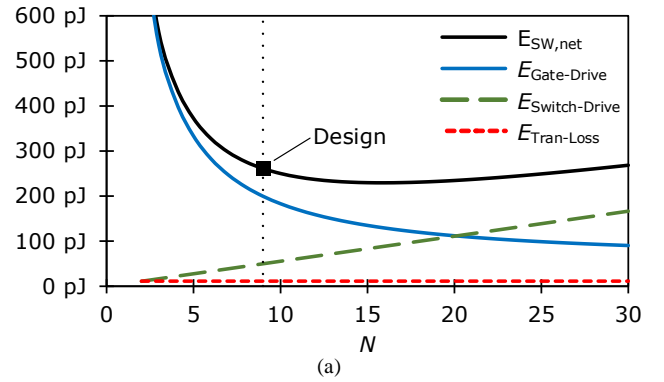


Fig. 14. Optimizing the energy losses of stepwise gate-drive for number of steps  $N$  (a), total  $v_{G1}$  fall-time  $T_F$  (b) and  $S_F$  switch resistance  $R_{SF}$  (c). When not swept:  $N = 9$ ,  $T_F = 1.3$   $\mu$ s,  $R_{SF} = 120$   $\Omega$  (the values used in the design).

$$E_{SW,net} = E_{Gate-Drive} + E_{Switch-Drive} + E_{Tran-Loss}, \quad (31)$$

where  $E_{Gate-Drive}$  is calculated from (4)–(13),  $E_{Switch-Drive}$  is calculated from (15) ( $\rho = 670 \text{ pJ-}\Omega$ ), and  $E_{Tran-Loss}$  uses the simulated data of Fig. 9. The total  $v_{G1}$  transition time  $T_F$  is a function of step duration  $T_{SF}$  and number of steps  $N$ :

$$T_F = NT_{SF}. \quad (32)$$

$C_{Tank}$  should be as large as possible for the available die area, with  $C_{Total}$  being the total capacitance that can fit on the die:

$$C_{Total} = (N - 1)C_{Tank}. \quad (33)$$

Fig. 14 shows  $E_{SW,net}$  and its components plotted against  $N$ ,  $R_{SF}$ , and  $T_F$ . Since the rising edge of  $v_{G1}$  does not have a significant effect on transition losses,  $T_R$ ,  $T_{SR}$ , and  $R_{SR}$  were omitted from the optimization algorithm. Instead, the resistance of rising-edge switches  $S_R$  was set to be  $R_{SR} = 8R_{SF}$ , and the total  $v_{G1}$  rise-time was set to be  $T_R = 70T_F$ , giving ample time for settling.

## IX. MEASURED RESULTS

Fig. 15 shows the DC-DC converter circuit, including a micrograph of the integrated circuit (IC). A TEG is connected to the input. The IC was fabricated in a 600-nm CMOS process, which was chosen for having lower leakage current than CMOS processes of smaller feature sizes. The circuit has ten 3.9 mF capacitors for  $C_{IN}$ , for an input ripple voltage of  $\pm 2.5\%$  and a combined capacitor equivalent series resistance (ESR) of 0.8 m $\Omega$ . Using just one capacitor would be tolerable but would result in reduced efficiency due to higher input voltage ripple and ESR.  $C_{OUT}$  has seven 47  $\mu\text{F}$  capacitors to deliver 170  $\mu\text{J}$  of energy to the load for each pulse of the *power good* signal. Capacitors rated at 100 V were selected for  $C_{OUT}$  because they have a combined capacitor leakage of just 50 pA. The flyback transformer has 6 turns on the primary and 120 turns for each secondary winding. The primary winding has an inductance of 300  $\mu\text{H}$  with a resistance of 5 m $\Omega$ . Each secondary winding has a resistance of 11  $\Omega$ . The power FET  $M_1$  has a resistance of 34 m $\Omega$  at  $V_{OUT} = 2.5 \text{ V}$ .  $M_{2P}/M_{2N}$  on-resistance is  $R_{on2} = 6 \Omega$ .

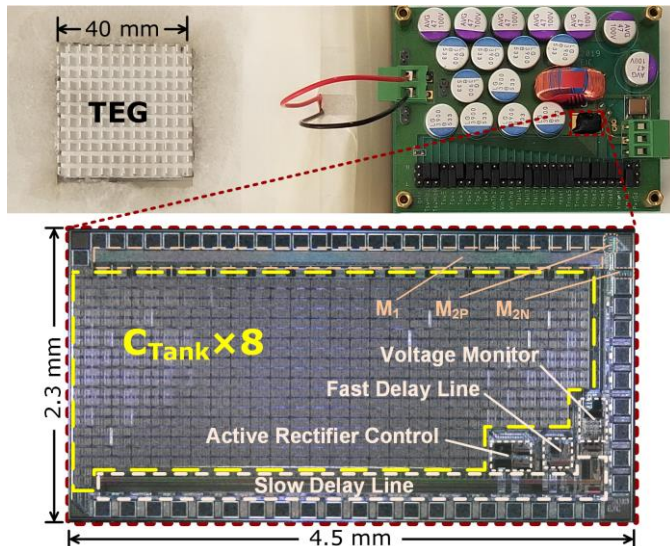


Fig. 15. Photograph of the DC-DC converter connected to a TEG [45] that is sandwiched between an insulated aluminum block and a heat sink.

### A. Efficiency and Input Impedance

Fig. 16 shows the measured efficiency and input impedance (defined as  $V_{IN} / I_{IN}$ ) of the DC-DC converter for input voltages from  $\pm 0.5 \text{ mV}$  to  $\pm 50 \text{ mV}$ . Efficiency and impedance are insensitive to input voltage polarity. The impedance is insensitive to  $V_{IN}$  for most of the range, decreasing as  $|V_{IN}|$  approaches 50 mV due to transformer saturation—effectively clamping  $|V_{IN}|$  at 50 mV. The 0% efficiency points were measured to be at  $V_{IN} = 0.487 \text{ mV}$  and  $-0.493 \text{ mV}$ , with a measurement accuracy of  $\pm 4 \mu\text{V}$ . The efficiency at  $V_{IN} = 1 \text{ mV}$  is  $63.0\% \pm 0.4\%$ , and the peak efficiency is  $83.9\% \pm 0.2\%$  at  $V_{IN} = 6.25 \text{ mV}$ . The specified measurement accuracy takes into account system noise, voltage measurement precision (including thermoelectric offsets), and current sensing resistor accuracy and temperature sensitivity. Measurements were taken at a room temperature between  $17^\circ\text{C}$  and  $21^\circ\text{C}$ .  $V_{IN}$  was driven with a source resistance of 1  $\Omega$  to mimic that of a matched TEG.

Fig. 16 also includes what the efficiency would be without stepwise gate-drive. This is calculated by subtracting the simulated power savings due to stepwise gate-drive from the total output power and adding the power consumed by the stepwise driver control circuitry and the transition losses due to the slower gate edge rates of stepwise charging (details are provided in the next section). The calculated 0% efficiency point without stepwise gate-drive is at  $V_{IN} = 0.883 \text{ mV}$  while the measured efficiency at this voltage with stepwise is 56.9%. All other plots are with stepwise gate-drive enabled.

Fig. 17 provides the DC-DC converter efficiency for various output voltages. Fig. 18 shows how the input impedance changes with  $V_{OUT}$  and how the minimum input voltage ( $V_{IN}$

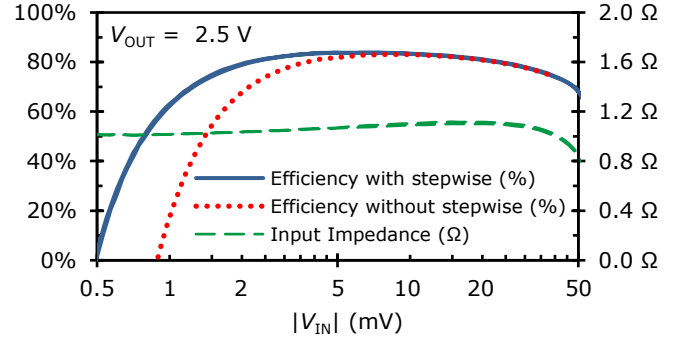


Fig. 16. DC-DC converter efficiency with and without stepwise gate drive and input impedance from  $-50 \text{ mV}$  to  $+50 \text{ mV}$  input voltage. Frequency set = 0 (350 Hz) and hibernation is disabled.

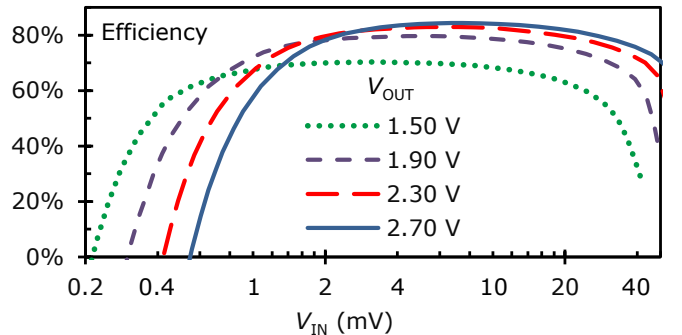


Fig. 17. Efficiency for  $V_{IN}$  ranging from  $+0.2 \text{ mV}$  to  $+50 \text{ mV}$  at various output voltages. Frequency set = 0 and hibernation is disabled.

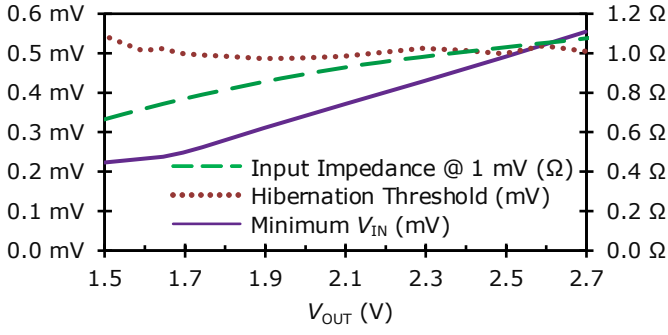


Fig. 18. Minimum  $V_{IN}$  ( $V_{IN}$  at efficiency = 0%; hibernation disabled), hibernation threshold ( $V_{IN,Th}$ ), and input impedance vs. output voltage.

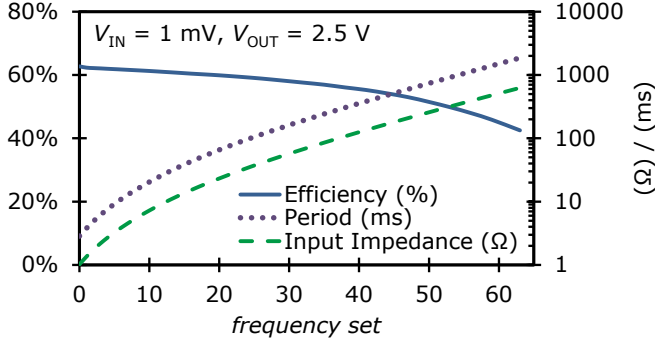


Fig. 19. The 6-bit input *frequency set* controls the switching period of the DC-DC converter. This sets Input impedance from 1  $\Omega$  to 600  $\Omega$ .

where the efficiency = 0%) aligns with the threshold at which the DC-DC converter enters hibernation,  $V_{IN,Th}$ . At  $V_{OUT} = 1.5$  V, the minimum  $V_{IN}$  is 0.223 mV. Ideally the hibernation threshold voltage would equal the minimum  $V_{IN}$  for all  $V_{OUT}$ , but delay line sensitivity to  $V_{OUT}$  causes them to diverge. Improvements in the bias generator in Fig. 5 could reduce the hibernation threshold divergence and the input impedance sensitivity to  $V_{OUT}$ ; however, since  $V_{OUT}$  is normally between 2.5 V and 2.7 V, these sensitivities are not particularly problematic.

The switching period of the DC-DC converter is programmable from 2.8 ms to 1.2 s through the 6-bit input *frequency set*. This allows the input impedance to be programmable from 1  $\Omega$  to 600  $\Omega$ , as shown in Fig. 19. Efficiency reduces with period as  $C_{OUT}$  leakage and the slow delay line consume more energy per cycle.

The minimum input voltage and total harvesting efficiency of this DC-DC converter could be improved significantly by implementing the adaptive frequency and on-time technique described in [5] by rebalancing the switching/conduction losses of  $M_1$  for low  $V_{IN}$ .

### B. Sources of Losses

Table I provides the sources of (simulated) energy losses within the DC-DC converter per cycle at  $V_{IN} = 1$  mV. The table also includes what the losses would be without stepwise gate-drive. The power consumption of the slow delay line and the fast delay line are included in the “without stepwise gate-drive” column because these circuits are still needed to generate the switching frequency and on-time for  $M_1$  and the reference delays for the input voltage detection and output voltage monitor. With *frequency set* = 0, the slow delay line utilizes 78

TABLE I  
SIMULATED ENERGY LOSSES PER SWITCHING CYCLE

Source of losses	With stepwise gate-drive		Without stepwise gate-drive	
	Energy losses	% of total losses	Energy losses	% of total losses
Stepwise gate driver for $M_1$	222 pJ	26.5%	1550 pJ	73.8%
Stepwise switch drivers	57 pJ	6.8%	0 pJ	0.0%
$M_1$ conduction losses	231 pJ	27.6%	231 pJ	11.0%
$M_1$ transition losses	10 pJ	1.2%	0 pJ	0.0%
$M_1$ drain capacitance losses	2 pJ	0.3%	2 pJ	0.1%
Gate driver for $M_2$	11 pJ	1.3%	11 pJ	0.5%
$M_2$ control & $V_{IN}$ detect	30 pJ	3.6%	30 pJ	1.4%
$M_2$ conduction losses	40 pJ	4.8%	40 pJ	1.9%
$M_2$ drain capacitance losses	63 pJ	7.5%	63 pJ	3.0%
Primary coil losses	34 pJ	4.1%	34 pJ	1.6%
Secondary coil losses	14 pJ	1.7%	14 pJ	0.7%
Slow delay line	45 pJ	5.4%	45 pJ	2.1%
Fast delay line	45 pJ	5.3%	45 pJ	2.1%
Voltage monitor	29 pJ	3.5%	29 pJ	1.4%
Other losses	4 pJ	0.5%	4 pJ	0.2%
Total input energy ( $E_{IN}$ )	2575 pJ		2575 pJ	
Total output energy ( $E_{OUT}$ )	1738 pJ		476 pJ	
Total losses ( $E_{IN} - E_{OUT}$ )	837 pJ		2099 pJ	
Simulated efficiency	67.5%		18.5%	

dly stages and consumes 45 pJ per cycle.

The stepwise gate driver losses ( $E_{Gate-Drive}$ ) of 222 pJ are calculated from the total charge that flows through switch  $S_{R9}$  per cycle ( $i_{SR9}$  in Fig. 3). This energy would be 1550 pJ without stepwise gate-drive. The ideal gate-drive energy consumption from (3) is 172 pJ. Of this 50 pJ difference, 30 pJ were found to be due to the  $C_{Tank} / C_{Gate}$  ratio (simulating with  $C_{Tank}$  6 $\times$  larger reduces the stepwise gate driver energy to 202 pJ). The remaining 20 pJ difference between simulated and ideal energy consumption is unaccounted for. Increasing settling time for each step, eliminating the Miller effect [40] by setting  $V_{IN} = 0$  mV, and reducing overlap between on-time for switches  $S_R$  and  $S_F$  (break-before-make) all had a negligible effect on the simulated energy consumption. The authors did find that the 20 pJ of unaccounted-for losses only appear when parasitic on-chip routing capacitance is included in the simulation, suggesting that those losses could be reduced with more efficient trace routing.

The transition losses due to the slower edge rates for  $v_{G1}$  ( $E_{Tran-Loss}$ ) are calculated to be 10 pJ and the stepwise switch drivers ( $E_{Switch-Drive}$ ) consume 57 pJ combined, showing that stepwise gate-drive saves a total of 1261 pJ: 49% of the total input energy  $E_{IN}$ . Total gate-drive energy is reduced by 82%. Even if the delay line circuits were included in the calculation, the net energy savings would be 1171 pJ: 45% of  $E_{IN}$ .

$M_2$  conduction losses of 40 pJ are dominated by the voltage drop of the body diode during the short period of time that  $M_2$  is conducting but  $v_{G2}$  is low, depicted in Fig. 11. The  $M_2$  on-resistance only contributes 1 pJ toward conduction losses.  $M_2$  drain capacitance losses includes all parasitic capacitance on nodes  $v_{D2P}$  and  $v_{D2N}$  including circuit board capacitance.

### C. Circuit Waveforms

Fig. 20 shows the captured waveforms of the fabricated circuit, including the captured stepwise gate voltage  $v_{G1}$ . The non-linear slope of  $i_1$  when  $V_{IN} = 50$  mV is due to transformer saturation. Fig. 21 shows the slow discharge of the output voltage during hibernation. When  $V_{IN} = 0$  mV and  $V_{OUT} = 2.5$



$V$ , the quiescent power that the converter draws from its output is  $255 \text{ pW} \pm 5 \text{ pW}$  (including the leakage of  $C_{\text{OUT}}$ ). The low power consumption keeps  $V_{\text{OUT}}$  above the minimum required voltage of  $1.5 \text{ V}$  for 12 weeks, meaning that after initial startup the DC-DC converter would only need to be revived if there was no input power for a 12-week duration. Otherwise, a cold-start circuit like the  $11\text{-mV}$  one in [35] could be used.

Fig. 21 also shows the function of the *power good* signal as  $V_{\text{OUT}}$  completes charge cycles. The output voltage rises as the DC-DC converter draws power from the  $1 \text{ mV}$  source. Once  $V_{\text{OUT}}$  rises above  $2.7 \text{ V}$ , *power good* is set high. In this experiment there is no external load on the DC-DC converter; the voltage monitor consumes  $10 \text{ }\mu\text{W}$  of power while *power good* is high, causing  $V_{\text{OUT}}$  to discharge until reaching  $2.5 \text{ V}$ .

Fig. 22 shows the converter functioning in a complete energy harvesting system, connected to the TEG [45] shown in Fig. 15. The TEG has an insulated aluminum block on side and a heat sink on the other side, similar to [14], but without the phase-change material.  $R_{\text{TEG}}$  was measured to be  $9 \text{ }\Omega$  and the DC-DC converter input impedance was programmed to be  $13 \text{ }\Omega$ —slightly higher than  $R_{\text{TEG}}$  to improve total harvesting efficiency [5]. Room temperature is fluctuating by approximately  $\pm 1 \text{ }^\circ\text{C}$  and the temperature of the aluminum block lags that of the ambient air creating a small temperature difference. The  $\Delta T$  across the TEG itself was not measured but is expected to be much less than the difference between the aluminum block and the ambient air. The average  $V_{\text{IN}}$  per air-to-block temperature difference is  $2.6 \text{ mV}/^\circ\text{C}$  (excluding time in hibernation) and  $V_{\text{OUT}}$  is visibly charging for  $|V_{\text{IN}}|$  as low as  $0.6 \text{ V}$  (for both polarities). The *power good* pin is loaded with a  $1 \text{ k}\Omega$  resistor. The average output power was calculated to be  $24 \text{ nW}$ , based on the charging rate of  $C_{\text{OUT}}$ .

#### D. Comparison with Other Work

Table II compares performance with other work. The minimum  $V_{\text{IN}}$  of  $\pm 0.5 \text{ mV}$  is ten times lower than the bipolar converter in [16] and seven times lower than the unipolar converter in [5]. The quiescent power of  $255 \text{ pW}$  is surpassed only by [38], which has a minimum input voltage of  $250 \text{ mV}$ , much higher than the  $\pm 0.5 \text{ mV}$  of this work.

#### X. CONCLUSION

A step-up DC-DC converter that leverages a stepwise gate driver to achieve a minimum input voltage of  $\pm 0.5 \text{ mV}$  was presented. A low-power delay line circuit efficiently provides the timing signals needed by the stepwise gate driver while also providing timing for on-time, switching frequency, and input voltage detection. The converter hibernates when the input voltage is too low—reducing quiescent power to just  $255 \text{ pW}$ . An extra winding on the flyback transformer enables bipolar operation for harvesting energy from both positive and negative temperature differentials. A closed-form analytical model of stepwise gate-drive energy for efficiency optimization was presented. The converter was deployed in an energy harvesting system that harvesting thermoelectric energy from air temperature fluctuations less than  $1^\circ\text{C}$ .

#### ACKNOWLEDGMENTS

The authors would like to acknowledge the following individuals for their contributions to this work: Nick Purcell,

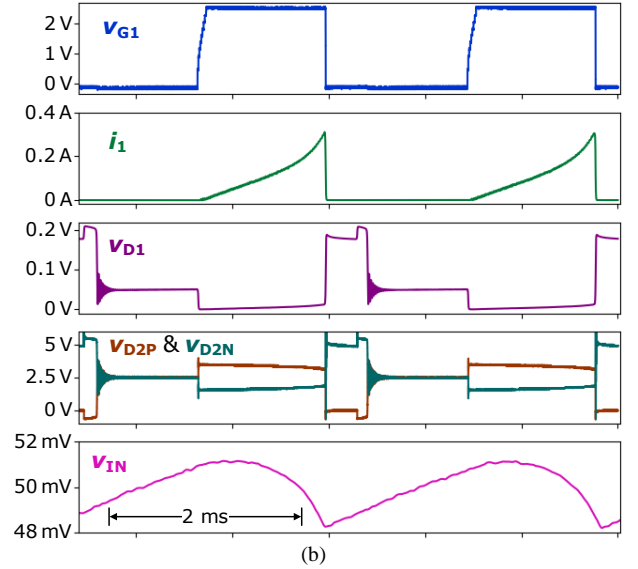
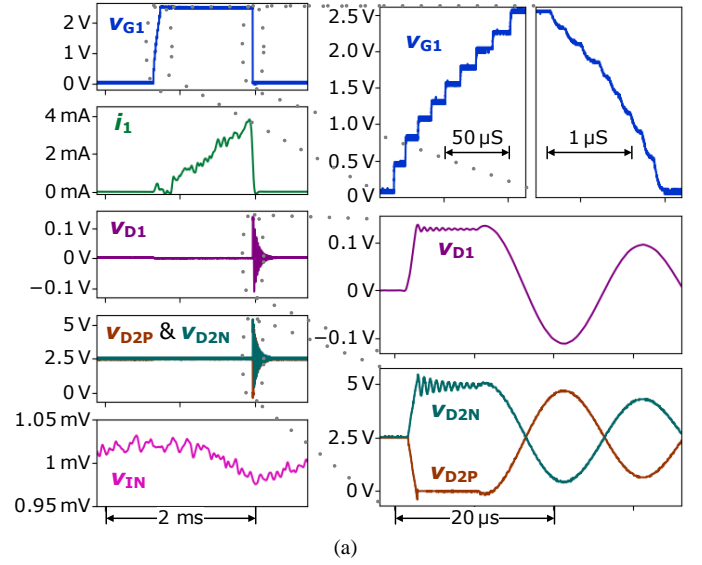


Fig. 20. Captured DC-DC converter circuit waveforms for  $V_{\text{IN}} = 1 \text{ mV}$  (a) and  $V_{\text{IN}} = 50 \text{ mV}$  (b).  $V_{\text{OUT}} = 2.5 \text{ V}$ . Frequency set = 0.

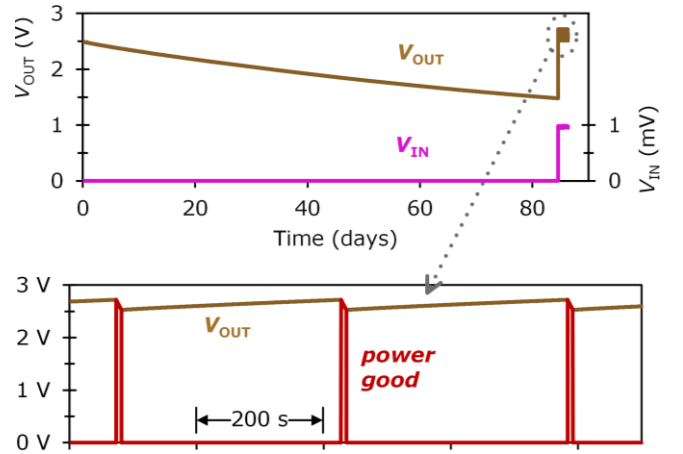


Fig. 21. The DC-DC converter recovers after 84 days of zero input voltage (top). When  $1 \text{ mV}$  is applied to the input the output charges up to  $2.7 \text{ V}$ , enabling the *power good* signal (bottom) until  $V_{\text{OUT}}$  drops below  $2.5 \text{ V}$ , after which the output charges back to  $2.7 \text{ V}$  to complete the cycle.



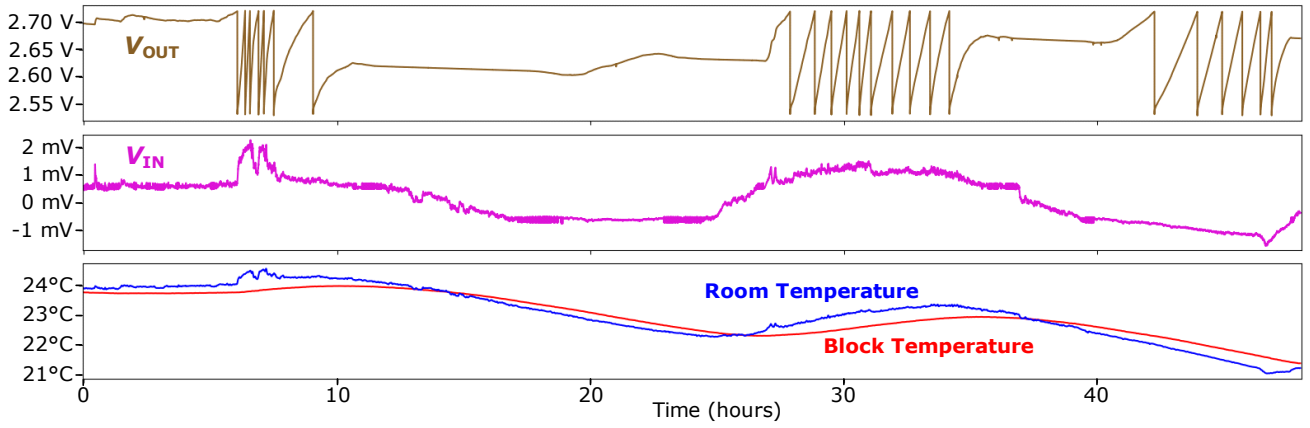


Fig. 22. Voltage and temperature waveforms of the DC-DC converter connected to a TEG [45] with heat sink and aluminum block as shown in Fig. 5, indoors.

TABLE II  
PERFORMANCE COMPARISON WITH OTHER WORK

	[5]	[6]	[19]	[16]	[18]	[20]	[38]	[46]	This Work
Input Voltage Range	3.5 mV – 100 mV	$\pm 20$ mV – $\pm 50$ mV	$\pm 25$ mV – $\pm 300$ mV	$\pm 5$ mV – $\pm 200$ mV	$\pm 13$ mV – $\pm 1$ V	$\pm 30$ mV – $\pm 500$ mV	250 mV – 650 mV	20 mV – 72 mV	$\pm 0.5$ mV – $\pm 50$ mV
Bipolar Input?	No	Yes	Yes	Yes	Yes	Yes	No	No	Yes
Output Voltage	1.2 V	1.2 V	1 V	2.0 V – 4.2 V	3 V – 5 V	2.35 V – 5 V	4.0 V	1.1 V	2.5 V
Quiescent Power	240 nW	N/R	N/R	N/R	N/R	16 $\mu$ W	20 pW	544 pW	255 pW
Peak Efficiency	82%	70%	84%	61%	85%	55%	60%	55%	84%
CMOS Process	180 nm	65 nm	180 nm	N/R	N/R	N/R	180 nm	180 nm	600 nm

N/R: Not reported

James Stevens, and Matthew Dillingham for assistance in circuit fabrication; Body Mahoney for CAD support; Jay Rajagopalan and Visvesh Sathe for manuscript review and feedback.

#### REFERENCES

- [1] L. L. Baranowski, G. J. Snyder and E. S. Toberer, "Effective thermal conductivity in thermoelectric materials," *J. Appl. Phys.*, vol. 113, no. 20, pp. 105–114, May 2013.
- [2] E. J. Carlson, K. Strunz and B. P. Otis, "A 20 mV input boost converter with efficient digital control for thermoelectric energy harvesting," *IEEE J. Solid-State Circuits*, vol. 45, no. 4, pp. 741–750, Apr. 2010.
- [3] E. J. Carlson, K. Strunz and B. P. Otis, "Erratum to "A 20 mV input boost converter with efficient digital control for thermoelectric energy harvesting" [Apr 10 741-750]," *IEEE J. Solid-State Circuits*, vol. 56, no. 1, pp. 324–324, Jan. 2021.
- [4] Y. K. Ramadass and A. P. Chandrakasan, "A battery-less thermoelectric energy harvesting interface circuit with 35 mV Startup Voltage," *IEEE J. Solid-State Circuits*, vol. 46, no. 1, pp. 333–341, Jan. 2011.
- [5] S. Bose, T. Anand and M. L. Johnston, "A 3.5-mV input single-inductor self-starting boost converter with loss-aware MPPT for efficient autonomous body-heat energy harvesting," *IEEE J. Solid-State Circuits*, vol. 56, no. 6, pp. 1837–1848, June 2021.
- [6] M. Alhawari, B. Mohammad, H. Saleh and M. Ismail, "An efficient polarity detection technique for thermoelectric harvester in L-based converters," *IEEE Trans. Circuits Syst. I, Reg. Papers*, vol. 64, no. 3, pp. 705–716, Mar. 2017.
- [7] C. Souza, F. Carvalho, F. Silva, H. Andrade, N. Silva and O. Baiocchi, I. Muller, "On harvesting energy from tree trunks for environmental monitoring," *Int. J. of Distributed Sensor Networks*, June 2016.
- [8] C. T. Hsu, G. Y. Chu, H. S. Chu, B. Yu and D. J. Yao, "Experiments and simulations on low-temperature waste heat harvesting system by Thermoelectric Power Generators," *Applied Energy*, vol. 88, no. 4, pp. 1291–1297, Apr. 2011.
- [9] A. Moser, M. Erd, M. Kostic, K. Cobry, M. Kroener and P. Woias, "Thermoelectric energy harvesting from transient ambient temperature gradients," *J. Electron. Mater.*, vol. 41, pp. 1653–1661, Feb. 2012.
- [10] L. Sigrist, N. Stricker, D. Bernath, J. Beutel and L. Thiele, "Thermoelectric energy harvesting from gradients in the Earth surface," *IEEE Trans. Ind. Electron.*, vol. 67, no. 11, pp. 9460–9470, Nov. 2020.
- [11] S. A. Whalen and R. C. Dykhuizen, "Thermoelectric energy harvesting from diurnal heat flow in the upper soil layer," *Energy Conversion and Management*, vol. 64, pp. 397–402, Dec. 2012.
- [12] E. E. Lawrence and G. J. Snyder, "A study of heat sink performance in air and soil for use in a thermoelectric energy harvesting device," in *21<sup>st</sup> Int. Conf. on Thermoelectrics*, 2002, pp. 446–449.
- [13] S. Pullwitt, U. Kulau, R. Hartung and L. Wolf, "A feasibility study on energy harvesting from soil temperature differences," in *7<sup>th</sup> Int. Workshop on Real-World Embedded Wireless Systems and Networks*, 2018, pp. 1–6.
- [14] M. E. Kiziroglou, S. W. Wright, T. T. Toh, P. D. Mitcheson, T. Becker and E. M. Yeatman, "Design and fabrication of heat storage thermoelectric harvesting devices," *IEEE Trans. Ind. Electron.*, vol. 61, no. 1, pp. 302–309, Jan. 2014.
- [15] G. Verma and V. Sharma, "A novel thermoelectric energy harvester for wireless sensor network application," *IEEE Trans. Ind. Electron.*, vol. 66, no. 5, pp. 3530–3538, May 2019.
- [16] EM Microelectronic, "Ultra-low voltage DCDC boost converter for thermal electrical generators," *EM8900 datasheet*, Mar. 2017.
- [17] A. Dancy, "Power supplies for ultra low power applications," M.S. Thesis, Dept. of Electrical Eng. and Computer Science, MIT, Boston, MA, 1996.
- [18] H. Dillersberger, B. Deutschmann and D. Tham, "A bipolar  $\pm 13$  mV self-starting and 85% peak efficiency DC/DC converter for thermoelectric energy harvesting," *Energies*, vol. 13, no. 20, Oct. 2020.
- [19] P. Cao, Y. Qian, P. Xue, D. Lu, J. He and Z. Hong, "A bipolar-input thermoelectric energy-harvesting interface with boost/flyback hybrid converter and on-chip cold starter," *IEEE J. Solid-State Circuits*, vol. 54, no. 12, pp. 3362–3374, Dec. 2019.
- [20] Analog Devices, "Auto-polarity, ultralow voltage step-up converter and power manager," *LTC3109 datasheet*, 2010.
- [21] K. Roy, S. Mukhopadhyay and H. Mahmoodi-Meimand, "Leakage current mechanisms and leakage reduction techniques in deep-submicrometer CMOS circuits," in *Proc. Of the IEEE*, vol. 9, no. 2, pp. 305–327, Feb. 2003.
- [22] H. Fujita, "A resonant gate-drive circuit capable of high-frequency and high-efficiency operation," *IEEE Trans. Power Electron.*, vol. 25, no. 4, pp. 962–969, Apr. 2010.
- [23] L. J. Svensson and J. G. Koller, "Driving a capacitive load without dissipating fCV<sup>2</sup>," *IEEE Symp. Low Power Electronics Dig. Tech. Papers.*, Oct. 1994, pp. 100–101.
- [24] L. J. Svensson and J. G. Koller, "Adiabatic charging without inductors," USC/ISI technical report ACMOS-TR-3a, Feb. 1994.

- [25] M. van Elzakker, E. van Tuijl, P. Geraedts, D. Schinkel, E. A. M. Klumperink and B. Nauta, "A 10-bit charge-redistribution ADC consuming 1.9  $\mu$ W at 1 MS/s," *IEEE J. Solid-State Circuits*, vol. 45, no. 5, pp. 1007–1015, May 2010.
- [26] A. Khorami and M. Sharifkhani, "General characterization method and a fast load-charge-preserving switching procedure for the stepwise adiabatic circuits," *IEEE IEEE Trans. Circuits Syst. I, Reg. Papers*, vol. 63, no. 1, pp. 80–90, Jan. 2016.
- [27] M. Arsalan and M. Shams, "Charge-recovery power clock generators for adiabatic logic circuits," in *18th Int. Conf. on VLSI Design*, 2005, pp. 171–174.
- [28] J. Park, Y.-H. Hwang, J. Oh, Y. Song, J.-E. Park and D.-K. Jeong, "A mutual capacitance touch readout IC with 64% reduced-power adiabatic driving over heavily coupled touch screen," *IEEE J. Solid-State Circuits*, vol. 54, no. 6, pp. 1694–1704, Jun. 2019.
- [29] F. Veirano, P. C. Lisboa, P. Perez-Nicoli, L. Naviner, F. Silveira, "Analysis of stepwise charging limits and its implementation for efficiency improvement in switch capacitor DC-DC converters," *Analog Integr Circ Sig Process*, vol. 109, pp. 271–282, Nov. 2021.
- [30] A. Khorami and R. Saeidi, "Energy consumption analysis of the stepwise adiabatic circuits," *Microelectronics Journal*, vol. 104, Oct. 2020.
- [31] E. J. Carlson and J. R. Smith, "An analytical model for stepwise adiabatic driver energy consumption," *TBD*.
- [32] T. B. Cho and P. R. Gray, "A 10 b, 20 Msample/s, 35 mW pipeline A/D converter," *IEEE J. Solid-State Circuits*, vol. 30, no. 3, pp. 166–172, Mar. 1995.
- [33] A. M. Abo and P. R. Gray, "A 1.5-V, 10-bit, 14.3-MS/s CMOS pipeline analog-to-digital converter," *IEEE J. Solid-State Circuits*, vol. 34, no. 5, pp. 599–606, May 1999.
- [34] J. Rabaey, A. Chandrakasan and B. Nikolić, "The devices," in *Digital Integrated Circuits: A Design Perspective*, 2<sup>nd</sup> Ed. Englewood Cliffs, NJ: Prentice-Hall, 2003, pp. 99–100.
- [35] R. L. Radin, M. Sawan, C. Galup-Montoro and M. C. Schneider, "A 7.5-mV-Input Boost Converter for Thermal Energy Harvesting With 11-mV Self-Startup," *IEEE Trans. Circuits Syst., II, Exp. Briefs*, vol. 67, no. 8, pp. 1379–1383, Aug. 2020.
- [36] Z. Luo, L. Zeng, B. Lau, Y. Lian and C. Heng, "A sub-10 mV power converter with fully integrated self-start, MPPT, and ZCS control for thermoelectric energy harvesting," *IEEE Trans. Circuits Syst. I, Reg. Papers*, vol. 65, no. 5, pp. 1744–1757, May 2018.
- [37] G. Chowdary and S. Chatterjee, "A 300-nW Sensitive, 50-nA DC-DC converter for energy harvesting applications," *IEEE Trans. Circuits Syst. I, Reg. Papers*, vol. 62, no. 11, pp. 2674–2684, Nov. 2015.
- [38] X. Wu, Y. Shi, S. Jeloka, K. Yang, I. Lee, Y. Lee and D. Sylvester, "A 20-pW Discontinuous switched-capacitor energy harvester for smart sensor applications," *IEEE J. Solid-State Circuits*, vol. 52, no. 4, pp. 972–984, Apr. 2017.
- [39] C. Chiang and C. Chen, "Zero-voltage-switching control for a PWM buck converter under DCM/CCM boundary," in *IEEE Trans. Power Electron.*, vol. 24, no. 9, pp. 2120–2126, Sep. 2009.
- [40] L. Balogh, "Design and application guide for high speed MOSFET gate drive circuits," in *Power Supply Design Seminar (SEM 1400)*, 2001.
- [41] J. N. Park and T. R. Zaloum, "A dual mode forward/flyback converter," *1982 IEEE Power Electronics Specialists conf.*, 1982, pp. 3–13.
- [42] B. Acker, C. R. Sullivan and S. R. Sanders, "Synchronous rectification with adaptive timing control," in *26th Annual IEEE Power Electronics Specialists Conf. Record, PESC'95*, Jun. 18–22, 1995, vol. 1, pp. 88.
- [43] R. L. Radin, M. Sawan and M. C. Schneider, "An accurate zero-current-switching circuit for ultra-low-voltage boost converters," *IEEE Trans. Circuits Syst., II, Exp. Briefs*, vol. 68, no. 6, pp. 1773–1777, Jun. 2021.
- [44] N. V. Desai, Y. K. Ramadass and A. P. Chandrakasan, "A bipolar  $\pm 40$  mV self-starting boost converter with transformer reuse for thermoelectric energy harvesting," in *2014 IEEE/ACM Int. Symp. Low on Power Electronics and Design (ISLPED)*, 2014, pp. 221–226.
- [45] TEC, *TEG2-126LDT datasheet*, Oct. 2017.
- [46] S. Bandyopadhyay, P. P. Mercier, A. C. Lysaght, K. M. Stankovic and A. P. Chandrakasan, "A 1.1 nW energy-harvesting system with 544 pW quiescent power for next-generation implants," *IEEE J. Solid-State Circuits*, vol. 49, no. 12, pp. 2812–2824, Dec. 2014.



**Eric J. Carlson** (Member, IEEE) received the B.S. and M.S. degrees in Electrical Engineering from the University of Washington, Seattle, WA, USA, in 2006 and 2008, respectively. He is currently a Ph.D. candidate at the University of Washington with a research focus in DC-DC converters and power management circuits for energy harvesting. He was a recipient of the Granger Foundation Fellowship and the Robert F. Rushmer fellowship.

Since 2007 he has been an analog circuit designer at Texas Instruments (formerly National Semiconductor) having worked in Mobile Devices Power, FPD-Link, and Clock & Timing Solutions product lines.



**Joshua R. Smith** (Fellow, IEEE) received the B.A. degree in computer science and philosophy from Williams College, Williamstown, MA, USA, in 1991, the M.A. degree in physics from the University of Cambridge, Cambridge, U.K., in 1997, and the S.M. and Ph.D. degrees from the Massachusetts Institute of Technology, Cambridge, MA, USA, in 1995 and 1999, respectively.

Before joining the University of Washington, Seattle, WA, USA, he was a Principal Engineer with Intel Corporation, Seattle. He is a Co-Founder of three companies that are commercializing research from his lab: Wibotic, Seattle, is applying near field resonant WPT for applications, such as recharging robots and powering implanted devices; Jeeva Wireless, Seattle, makes low power backscatter communication products; and Proprio, Seattle, provides surgical visualization and navigation technology. He is currently the Milton and Delia Zeitschel Professor, jointly appointed in the Allen School of Computer Science and Engineering and the Department of Electrical and Computer Engineering, with the University of Washington.